JOURNAL OF OPTOELECTRONICS AND ADVANCED MATERIALS Vol. 10, No. 8, August 2008, p. 1910 - 1916

Application of atmospheric pressure non-equilibrium plasma to nanomaterials synthesis

KEN OKAZAKI, TOMOHIRO NOZAKI*

Dept of Mechanical and Control Engineering, Tokyo Institute of Technology, 2-12-1O-okayama, Meguro, 1528552, Tokyo, Japan

This paper overviews our recent work which focus on bottom-up nanomaterials synthesis within the scope of atmospheric pressure glow discharge. First, high-purity SWCNTs are producible only when atmospheric pressure radio-frequency discharge was applied: even moderate pressure such as 20 kPa preferentially synthesized multi-walled CNTs. Although ion damage is avoided in highly collisional plasma sheathe, the excess supply of excited species accelerates undesired catalyst coagulation. Second, microplasma synthesis of tunable photoluminescent silicon nanocrystals (Si-NCs) is presented. A mixture of Ar, H_2, and $SiCl_4$ was activated by miniaturized capacitively-coupled non-equilibrium plasma generated in a capillary glass tube with a volume less than 1 μ-liter. Room temperature photoluminescence (PL) of as-produced material synthesized with H_2 = 0.7% exhibited visible red-photoluminescence (670 nm) without any posttreatment, while TEM analysis revealed 3 nm Si-NCs. The PL spectrum was monotonically blue-shifted until 520 nm with increasing hydrogen content in the feed gas (H_2 = 3%).

(Received March 1, 2008; accepted June 30, 2008)

Keywords: Atmospheric pressure non-equilibrium plasma, Microplasma, Nanotechnology, Carbon nanotubes, Silicon nanocrystals, Photoluminescence

1. Introduction

Recent remarkable progress in formation techniques of atmospheric pressure glow discharges (APG) lead to a promising new frontier with great potential to build up unique plasma processes: the APG is highlighted not only for improving productivity of industrial applications, but also for synthesis of functional materials. Because of their special advantages of forming reactive plasmas in a simple reactor, applications of atmospheric pressure non-equilibrium plasmas are spreading into various engineering fields such as surface treatment [1], chemical synthesis [2], aerodynamic actuators [3–5], biomedical sterilization [6–8], carbon nanotubes [9–11], amorphous carbon films [12], ultrahigh-speed etching [13], silicon nanoparticles [14,15], and amorphous/crystalline silicon films [16,17]. More recently, microplasma produced in a micrometer-sized reactor is also highlighted in association with atmospheric pressure non-equilibrium plasma because such small scale plasma inherently requires high-density media to initiate electrical breakdown [18,19]. This paper overviews our recent projects which focus on bottom-up nanomaterials synthesis within the scope of atmospheric pressure glow discharge [20]: (1) deposition of single-walled carbon nanotubes in atmospheric pressure radio-frequency discharge [11] and (2) microplasma synthesis of light-emitting silicon nanocrystals [15].

2. Single-walled carbon nanotube synthesis

Plasma enhanced chemical vapor deposition (PECVD) is recognized as one of the viable synthesis techniques for carbon nanotubes (CNTs) because free-standing vertically aligned CNTs are synthesized due to the electric field created in the plasma sheath. In addition, growth temperature is slightly lower than those found in thermal CVD regime. However, CNTs synthesized in low-pressure PECVD are overwhelmingly carbon nanofibers (CNFs) and multi-walled carbon nanotubes (MWCNTs) because catalysts and CNTs receive severe damage from ion bombardment [21]. Furthermore, excess supply of reactive species detrimentally produces amorphous carbon networks that readily deteriorate catalyst activity [21,22]. Tremendous interest in generation and characterization of SWCNTs and related applications has not arisen in the scope of PECVD until recently [23,24]. We proposed atmospheric pressure plasma enhanced chemical vapor deposition (AP-PECVD) for the synthesis of vertically aligned single-walled carbon nanotubes (SWCNTs), because both ion-damage and radical-damage to the SWCNTs are inherently avoided in highly collisional plasma sheath generated at atmospheric pressure [11]. It is noteworthy from the practical point of view that atmospheric pressure processing is beneficial to improve productivity with minimum cost and energy consumption because it reduces the needs for vacuum systems and enables to handle bulk materials in a continuous process. The comprehensive description of carbon nanotube synthesis in atmospheric pressure glow discharge will appear in the recent review paper [25].

2.1 Experimental

The SWCNTs were synthesized in the atmospheric pressure radio-frequency discharge (APRFD) reactor, which has been described in detail in ref [11]. Briefly, a schematic diagram of APRFD reactor is shown in Fig. 1. The APRFD is produced between two parallel-plate metallic electrodes of 4 cm diameter with 5 mm separation. A radio-frequency (13.56 MHz) power source was connected to the upper electrode. The substrates were loaded on the heated bottom electrode. The chamber was evacuated to 1.3 Pa, then a mixture of helium, hydrogen, and methane was introduced from the upper electrode equipped with a water-cooled shower head. We prepared densely monodispersed Fe-Co nanoparticles on a silicon substrate by dip-coating method. See ref [26] for detailed preparation procedure. Metallic catalyst particles and bare silicon substrates were isolated by a thin alumina layer, which also enhances catalytic activity of the metallic particles. Basic conditions in this report are as follows unless otherwise specified: $He/H_2/CH_4$, 1000/30/16 cm^3 min^{-1}; power, 60 W; deposition time, 5 min; substrate temperature, 700°C; pressure, 108 kPa. The CNTs were characterized by Raman spectroscopy with 532 nm laser (NRS-2100, JASCO), scanning electron microscope (S-800, HITACHI), and transmission electron microscope operated at 200 kV (JEM-310, JEOL).

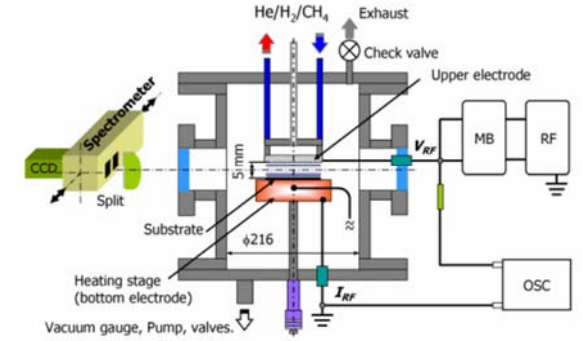

Fig. 1 Schematic of the APRFD reactor.

2.2 Analysis of SWCNTs and growth regime

A typical example of vertically aligned SWCNTs is presented in Fig 2. The SWCNTs were deposited uniformly with height of 60 μm on a 2-inch silicon substrate after 20 min synthesis. Figure 3 represents well-oriented SWCNT bundles due to van der Waals' force. Low-frequency Raman spectra shown in Fig. 2 inset exhibit radial breathing mode (RBM) spectrum between 150 cm^{-1} and 250 cm^{-1}. Diameters of SWCNTs were between 1 nm and 2 nm, as estimated using the following equation.

$$d_{SWCNT} = \frac{248}{\omega_{RBM}} \quad (1)$$

Here, d_{SWCNT} [nm] is the diameter of SWCNTs and ω_{RBM} [cm^{-1}] is the wave number of RBM [27]. The D-band peak attributes to either amorphous carbon or internal defects of graphite structure is small, implying that the as-produced material consists of high-purity SWCNTs with trace amount of amorphous carbon and defects. In the case of SWCNTs, due to their small diameter, a tangential vibration of graphite (~1585 cm^{-1}) splits into the transverse optical (G-) and the longitudinal optical (G+) modes [28]. In addition to RBM, the existence of G+ and G- peaks is the strong evidence that high purity SWCNTs were synthesized. The frequency and the half-width of G- peak depend on chirality of SWCNT and the sample shown in Fig. 2 consists mostly of semiconducting SWCNTs. The G- peak blue-shits and significantly broadened in the case of metallic SWCNTs: the G+ is independent of chirality. We also analyzed cross-section Raman spectrum in the low-frequency region as described in the inset of Fig. 2. The intensity of RBM gradually decreases as the measurement point moves from the top to the bottom of CNT film, implying that SWCNTs gradually transit to MWCNTs. Even if catalyst poisoning by carbon is absent, catalysts coagulate by sintering or undesired catalyst interaction with alumina buffer layer under high temperature condition [11]. The fact also implies that SWCNTs grow in the root growth regime where catalyst nanoparticles are anchored on the alumina buffer layer.

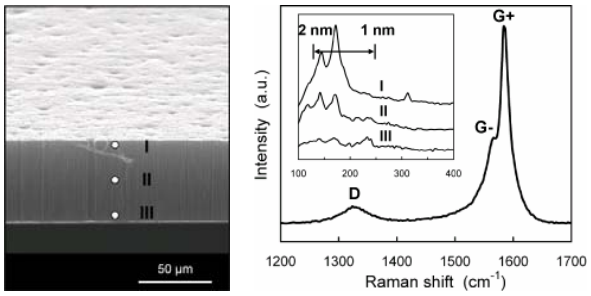

Fig. 2. Cross-section SEM micrograph and Raman spectra of SWCNTs.

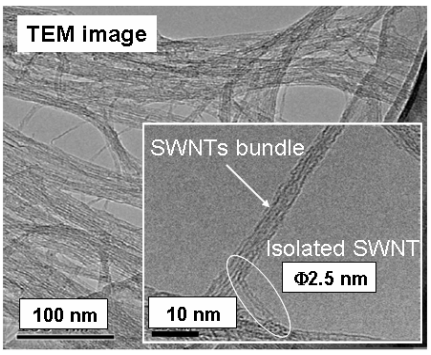

Fig. 3 High-resolution TEM micrograph of SWCNTs

2. 3 Reaction enhancement by APRFD and effect of the total pressure on SWCNT growth

The APRFD is beneficial for SWCNT growth because ion damage to the catalyst as well as CNTs is inherently avoided. Furthermore, it is believed to minimize the excess supply of reactive species which is responsible for over-growth of amorphous carbon network. To clarify the role of a highly collisional plasma sheath on SWCNT growth, we investigated the effect of total pressure from 110 kPa to 20 kPa. We also modified the gap separation from 5 mm to 10 mm according to the operating pressure.

Fig. 4 show SEM micrographs of CNTs synthesized at different power and total pressure. Corresponding Raman spectra are shown in Fig. 5. Figure 4 (a) and (b) clearly show that CNTs are synthesized only when the APRFD is applied; for the deposition condition and the catalyst used, thermal CVD growth of CNT was expected. However, carbon precipitation was not detected without APRFD. The application of APRFD engenders formation of reactive species in the negative glow that clearly enhances the growth process.

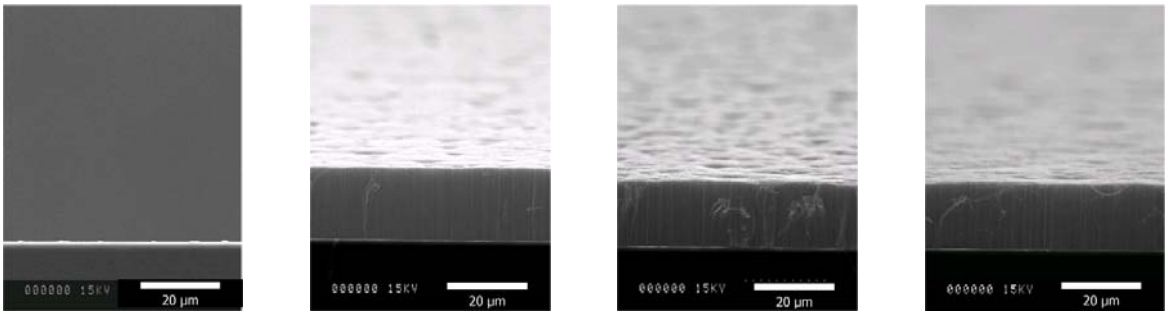

(a) 110 kPa − 0 W − 5 mm (b) 110 kPa − 60 W − 5 mm (c) 50 kPa − 60 W − 10 mm (d) 20 kPa − 60 W − 10 mm

Fig.4 SEM micrographs of CNTs synthesized at different power and total pressure

Raman spectra in Fig. 5 show that the defective band peak significantly increased at 20 kPa. Furthermore, the RBM frequencies, which corresponds to thinner SWCNTs (ca. 1.1 nm), disappeared, showing that CNFs or MWCNTs with less graphitization were synthesized under reduced pressure. The ion bombardment energy is estimated to be much smaller than 1 eV at 20 kPa, which is still low compared to the common low-pressure PECVD. Fig. 6 shows the high-resolution TEM micrograph and cross-section Raman spectrum of CNTs shown in Fig. 4(d); as-produced material in the reduced pressure (20 kPa) mainly consists of MWCNTs with 4−8 graphene sheets. The cross-section Raman spectrum revealed a large D-band peak from the top to the bottom of the CNT film; no SWCNTs could be identified. The excess supply of reactive species is well known to promote amorphous carbon formation. More important, it promotes catalyst coagulation that preferentially yields MWCNTs with large diameters.

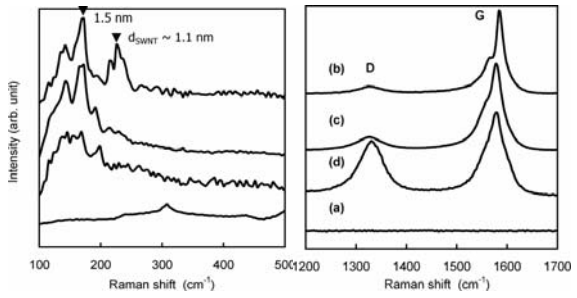

Fig. 5. Raman scattering spectra of CNTs synthesized at different total pressure.

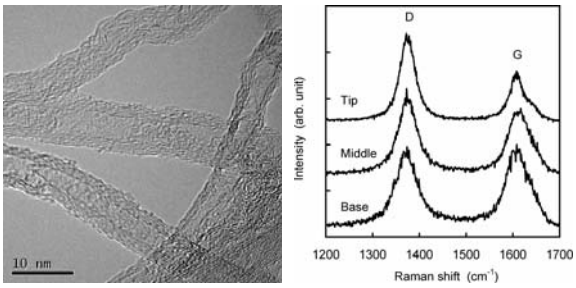

Fig. 6 High-resolution TEM micrograph and cross-section Raman scattering spectrum of MWCNTs

3. Microplasma synthesis of tunable photoluminescent silicon nanocrystals

Silicon nanocrystals (Si-NCs) with grain sizes of less than 5 nm are widely recognized as one of the key materials in optoelectronics, bio-imaging, and photovoltaic applications [29]. To date, several synthesis methods such as sputtering, laser ablation, and PECVD based on low-pressure processing have been established for synthesis of silicon nanostructured materials [30-33]. We propose microplasma approach as one of the viable synthesis techniques of tunable luminescent Si-NCs. An atmospheric-pressure non-thermal plasma generated in a miniaturized reactor is known as microplasma [18,19], and frequently characterized as high-density non-equilibrium plasma whose electron density increases greater than 10^{15}

cm^{-3} while electron temperature (> 10000 K) is much higher than gas temperature (< 2000 K) [34,35]. In such high density reactive plasma, the silicon precursor can be fully decomposed to create supersaturated silicon vapor, followed by fast crystal nucleation via three-body collision in the gas phase. Furthermore, excessive growth of silicon nuclei could be avoided in a short residence time reactor.

3-1. Microplasma principle and experimental

Fig. 7 schematically shows the experimental setup. Metallic electrodes were located outside of a capillary tube (Borosilicate glass: I.D. 630 μm, O.D. 1100 μm) with 2 mm separation. A very high frequency (144 MHz) power source was connected to the upper electrode via a matching circuit. Argon was used as carrier gas and a mixture of hydrogen and silicon tetrachloride was premixed before the microplasma reactor. The reactor was installed in a steel chamber to avoid air exposure which readily oxidizes as-produced material. A 15 mm square Corning glass substrate, which was coated with a chromium thin film, was located 30 mm downstream from the exit of the capillary tube. Synthesis conditions in this report are as follows: argon flow rate: 200 cm^3 min^{-1}, discharge power: 35 W, $SiCl_4$: 100 ppm. The Si-NCs were characterized by photoluminescence spectroscopy, SEM (S-800, HITACHI), and TEM (JEM-3010, JEOL). Optical emission spectroscopy of microplasma was also employed [36].

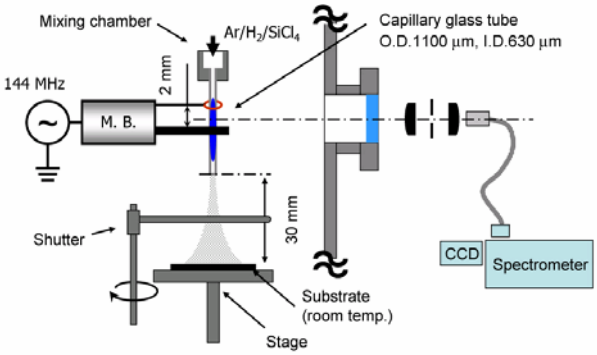

Fig. 7 Schematic diagram of the experimental setup.

3-2. Deposition rate

Fig. 8 shows microplasma photographic images observed at different hydrogen concentrations. The emission region extends outside both ends of metallic electrodes, but it gradually contracts as the hydrogen content increases. Electron density, estimated from Stark broadening of H_β line (486 nm), was initially 1×10^{15} cm^{-3} and decreased by 4×10^{14} cm^{-3} when H_2 = 3% because electrons lose their energy through excitation and dissociative collision with molecular hydrogen.

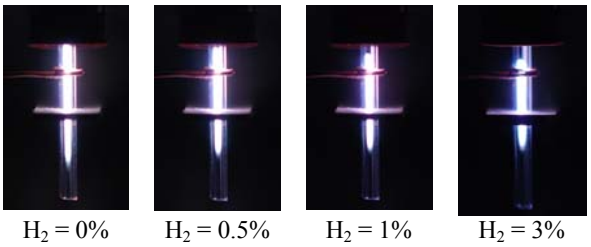

H_2 = 0% H_2 = 0.5% H_2 = 1% H_2 = 3%

Fig. 8 General appearance of the microplasma operated at different H_2 content. Ar flow rate: 200 cm^3min^{-1}, power: 35 W. $SiCl_4$ was not included.

Fig. 9 shows SEM micrographs of as-produced materials when hydrogen concentration was (a) 0% and (b) 0.7%, respectively. Deposition rate at H_2 = 0% was fairly slow. The TEM micrograph (Fig. 10(a)) reveals that the thin film actually consists of non-crystalline Si nanoparticles. On the other hand, the deposition rate remarkably increased as hydrogen content increased. Dense powder-like material was deposited at a rate of 3 μm min^{-1} when H_2 = 0.7% (Fig. 9(b)). Figure 10(b) displays crystalline particles with sizes around 3 nm and an amorphous silicon oxide shell which surrounds the crystalline core. Although electron density decreased with hydrogen increase, deposition rates increased because hydrogen-related reactive species efficiently abstract chlorine from $SiCl_n$ [37], and contribute to create supersaturated silicon vapor at given conditions. Atomic concentration of chlorine incorporated in as-produced materials, estimated by electron probe micro analyzer (JXA-8200, JEOL), was 0.5% at most.

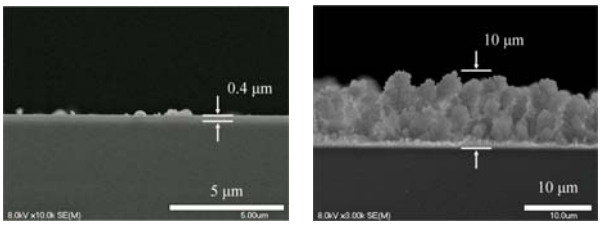

(a) H_2 = 0% (b) H_2 = 0.7%

Fig. 9. Cross-section SEM micrographs of as-synthesized material. Deposition time was 3 min for each sample.

3-3. Band gap energy of silicon nanocrystals

In order to correlate the crystal grain size and band gap energy with respect to initial hydrogen content, the room temperature photoluminescence (PL) was investigated. The 325 nm component of He-Cd laser was used as excitation light source and irradiated from normal to the substrate. The laser was spotted on 1 mm circular region. Visible photoluminescence was recorded in the back scattering geometry.

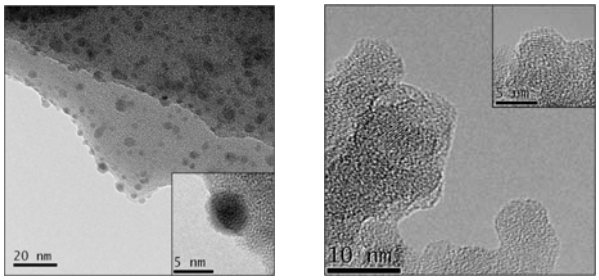

(a) H_2 = 0% (b) H_2 = 0.7%

Fig. 10 High-resolution TEM micrographs showing silicon nanoparticles.

Fig. 11 represents H_2-dependent changes in the room temperature PL spectrum of as-produced material. Faint visible emission was observed between H_2 = 0% and 0.5%. The PL intensity abruptly increased when H_2 = 0.7% with peak intensity at 670 nm. The PL spectrum slightly blue-shifted as initial hydrogen content increased, whereas PL intensity sharply dropped. The green-luminescent material centered at 520 nm was synthesized when H_2 > 2%. In general, quantum efficiency of Si-NCs with shorter wavelength is fairly low [38]. Therefore, deposition time was increased from 3 min to 15 min for green-luminescent materials (H_2 = 2−5%). In each case, a relatively narrow single PL spectrum was obtained with the FWHM of 95 nm at H_2 = 0.7% and 115 nm at H_2 = 3%. The PL intensity and corresponding wavelength of each spectrum provided in Fig. 11 are re-plotted in Fig. 12. The results clearly show that the peak wavelength monotonically decreased with hydrogen increase because increasing amount of hydrogen formed more silicon hydrides on the crystal surface, which in turn restrict further growth of silicon nuclei. In addition, according to the classical homogeneous nucleation theory, formation of silicon hydrides on clusters decreases the surface energy that also contributes to make smaller crystals. Crystal grain size with PL spectrum centered at 670 nm (H_2 = 0.7%) can be estimated to be 2.8 nm [39], which is well correlated with TEM analysis shown in Fig. 10(b). The green-luminescent Si-NCs should be much smaller than 2.8 nm; however, we could not assign crystal sizes from literature because predicted upper limit of emission energy of partially oxidized Si-NCs is 2.1 eV (590 nm) [39]. Furthermore, PL energy is determined by a surface state, and no longer as a function of crystal grain size if the size is smaller than 1.8 nm. The Si-NCs synthesized in the microplasma reactor are smaller than 3 nm and the size-controlled band gap tunability of as-produced material was possible between 750 nm (H_2 = 0%) and 520 nm (H_2 > 2%).

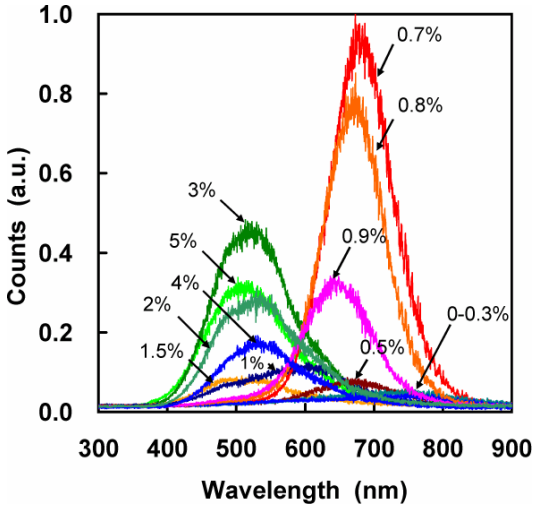

Fig. 11 Hydrogen dependent changes in PL spectrum. Deposition time was 3 min between H_2 = 0% and 1.5%, and 15 min between 2% and 5%, respectively.

3.4. Oxidation of silicon nanocrystals

As shown in Fig. 13, the PL intensity of red-luminescent material with a crystal size of 3 nm increased while peak wavelength remained unchanged during 24-hour natural oxidation in air. The Si-NCs with sizes around 3 nm are known to exhibit red-photoluminescence independent of surface oxide [39], therefore PL spectrum does not red-shift during oxidation. The Si=O double bond at the surface creates localized electronic states which probably work as an efficient radiative recombination center of electron-hole pair.

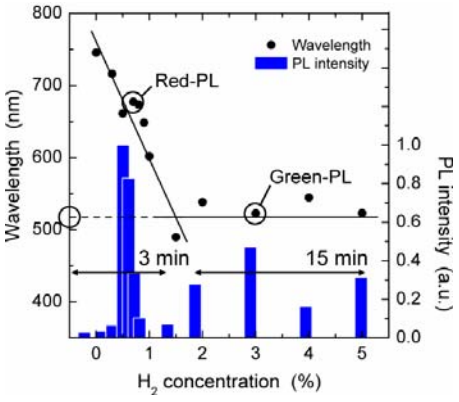

Fig. 12 Effect of hydrogen concentration on PL wavelength and emission intensity.

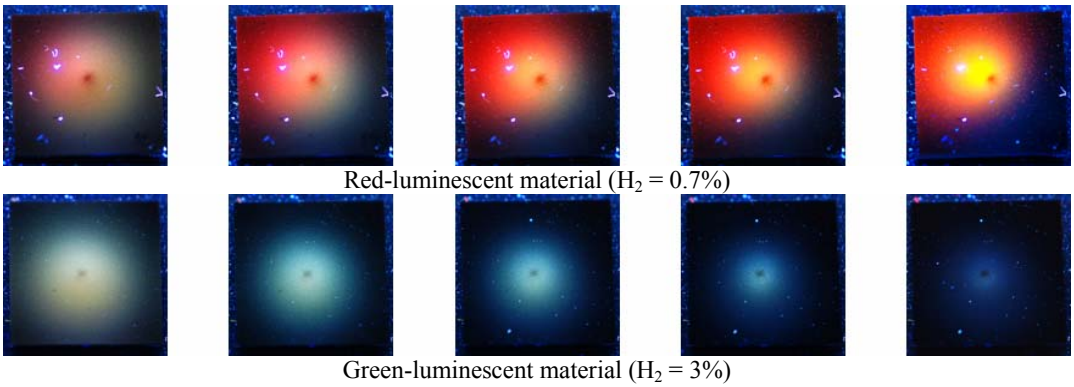

Fig. 13 Time-dependent changes in PL spectrum of red- and green-luminescent materials during natural oxidation in air. Each sample was deposited on 15 mm×15 mm silicon substrate. From left to right: as-grown (0h), 0.5 h, 1 h, 2 h, 24 h. The synthesized materials were excited by UV lamp (360 nm).

Oxidation of green-luminescent material exhibited a different trend. The material was already oxidized at the moment of PL measurement, therefore PL spectrum does not red-shift after oxidation. On the contrary, the PL spectrum blue-shifted until 450 nm as oxidation proceeded, and the PL intensity was rapidly degraded. Characterization of blue-luminescent Si-NCs is problematic because the predicted upper limit of emission energy of partially oxidized Si-NCs would be 2.1 eV and further downsizing of the crystal grain size only slightly contributes to enlarge optical emission gap. In green-luminescent material, the crystal grain size is so small that the nanocrystalline core is expected to shrink as surface oxidation proceeds. Accordingly, the PL spectrum gradually blue-shifts and its intensity declines. Blue emission may originate disordered structure of sub-stoichiometric silicon oxide network induced by Si nanocrystallite.

4. Concluding remarks

Synthesis of SWCNTs and Si-NCs using atmospheric pressure non-equilibrium plasma was introduced based on our recent work. High-purity vertically aligned SWCNTs were produced only when APRFD was applied, while no carbon deposition was detectable under the present conditions if APRFD was off. The application of APRFD engenders formation of reactive species in the negative glow that clearly enhances the growth process. On the other hand, moderate pressure (20 kPa) preferentially synthesized MWCNTs. Although ion bombardment energy at 20 kPa is much smaller than 1 eV, excess supply of reactive species accelerates undesired catalyst coagulation from the initial stage of CNT growth: Raman spectroscopy showed only MWCNTs from the top to the bottom of the CNT film. A continuous-flow, miniaturized non-thermal plasma reactor successfully synthesized tunable photoluminescent Si-NCs with sizes smaller than 3 nm. As-produced material synthesized with H_2 = 0.7% readily exhibited visible red-photoluminescence (670 nm) without any posttreatment such as high temperature annealing (> 1000 K). The PL spectrum was monotonically blue-shifted until 520 nm with increasing hydrogen content in the feed gas. Since PL capability of hydrogen-terminated Si-NCs is extremely sensitive against surface oxidation, in-flight plasma surface modification of Si-NCs with hydrocarbon ligand is now investigated.

Acknowledgements

The projects were supported by the Japanese Ministry of Education, Culture, Sports, Science and Technology Grants-in-Aid for Scientific Research by Priority Areas of Microplasmas (16040207) and Young Scientists (A) (18686018). We would like to thank Mr. Kuma Ohnishi, Tomohisa Ogino, and Takashi Nakamuta, graduate students of Tokyo Institute of Technology, for experimental support. Mr. Akira Genseki, Center for Advanced Materials Analysis of Tokyo Institute of Technology, supported TEM analysis.

References

[1] C. Tendero, C. Tixier, P. Tristant, J. Desmaison, P. Leprince, Spectrochimica Acta Part B **61**, 2 (2006).
[2] U. Kogelschatz, Plasma Chem. and Plasma Proc. **23**, 3 (2003).
[3] G. I. Font, W. L. Morgan, Contrib. Plasma. Phys. **47**, 103 (2007).
[4] A. Sasoh, K. Kikuchi, T. Sakai, J. Phys. D: Appl. Phys. **40**, 4181 (2007).
[5] E. Moreau, C. Louste, G. Artana, M. Forte, G. Touchard, Plasma Process. Polym. **3**, 697 (2006).
[6] E. Stoffels, Contrib. Plasma. Phys. **47**, 40 (2007).
[7] M. Laroussi, C. Tendero, X. Lu, S. Alla, W. L. Hynes, Plasma Process. Polym. **3**, 470 (2006).

[8] M. K. Boudam, M. Moisan, B. Saoudi, C. Popovici, N. Gherardi, F. Massines, J. Phys. D: Appl. Phys. **39**, 3494 (2006).
[9] T. Nozaki, Y. Kimura, K. Okazaki, J. Phys. D: Appl. Phys. **35**, 2779 (2002).
[10] T. Nozaki, T. Goto, K. Okazaki, K. Ohnishi, L. Mangolini, J. Heberlein, U. Kortshagen, J. Appl. Phys. **99**, 024310-1 (2006).
[11] T. Nozaki, K. Ohnishi, K. Okazaki, U. Kortshagen, Carbon **45**, 364 (2007).
[12] Y. Kondo, T. Saito, T. Terazawa, M. Saito, N. Ohtake, Jpn. J. Appl. Phys. **44**, L1573 (2005).
[13] K. Yamakawa, M. Hori, T. Goto, S. Den, T. Katagiri, H. Kano, J. Appl. Phys. **98**, 043311 (2005).
[14] N. Jidenko, C. Jimenez, F. Massines, J.-P. Borra, J. Phys. D: Appl. Phys. **40**, 4155 (2007).
[15] T Nozaki, K. Sasaki, T. Ogino, K. Okazaki, Nano technology **18**, 235603/1 (2007).
[16] H. Kakiuchi, H. Ohmi, Y. Kuwahara, M. Matsumoto, Y. Ebata, K. Yasutake, K. Yoshii, Y. Mori, Jpn. J. Appl. Phys. **45**(4B), 3587 (2006).
[17] H. Kitabatake, M. Suemitsu, H. Kitahata, S. Nakajima, T. Uehara, Y. Toyoshima, Jpn. J. Appl. Phys. **44**, L683 (2005).
[18] http://plasma.kuee.kyoto-u.ac.jp/tokutei429/ (consulted on 2008.Jan.31)
[19] K. H. Becker, K. H. Schoenbach, J. G. Eden, J. Phys. D: Appl. Phys. **39**, R55 (2006).
[20] T. Nozaki, K. Okazaki, Pure and Appl. Chem. **78**(6), 1147 (2006).
[21] A. V. Melechko, V. I. Merkulov, T. E. McKnight, M. A. Guillorn, K. L. Klein, D. H. Lowndes M. L. Simpsona, J. Appl. Phys. 97, 041301-1 (2005).
[22] M. Meyyappan, L. Delzeit, A. Cassell, D. Hash, Plasma Sources Sci. Technol. **12**, 205 (2003).
[23] T. Kato, R. Hatakeyama, K. Tohji, Nanotechnology **17**, 2223 (2006).
[24] G. Zhong, T. Iwasaki, J. Robertson, H. Kawarada, J. Phys. Chem. B Lett. **111**, 1907 (2007).
[25] T. Nozaki, K. Okazaki, Plasma Process. Polym., **5**, 300 (2008).
[26] Y. Murakami, Y. Miyauchi, S. Chiashi, S. Maruyama, Chem. Phys. Lett. **377**, 49 (2003).
[27] A. Jorio, R. Saito, J. H. Hafner, C. M. Lieber, M. Hunter, T. McClure, G. Dresselhaus, M. S. Dresselhaus, Phys. Rev. Lett., **86**, 1118 (2001).
[28] M. S. Dresselhaus, P. C. Eklund, Adv. Phys. **49**(6), 705. (2000)
[29] A. Puzder, A. J. Williamson, J. C. Grossman, G. Galli, J. Am. Chem. Soc., **125**(9), 2786. (2003).
[30] T. Makimura, T. Mizuta, K. Murakami, Jpn. J. Appl. Phys. **41**, L144 (2002).
[31] L. Xuegeng, H. Yuanqing, S. S. Talukdar, M. T. Swihart, Langmuir **19**, 8490 (2003).
[32] L. Mangolini, E. Thimsen, U. Kortshagen, Nano Letters **5**(4), 655 (2005).
[33] L. Mangolini, D. Jurbergs, E. Rogojina, U. Kortshagen, J. Luminescence **121**(2), 327 (2006).
[34] A. Kono, K. Iwamoto, Jpn J. Appl. Phys. **43**(8A), L1010 (2004).
[35] T. Ichiki, R. Taura, Y. Horiike, J. Appl. Phys. **95**(1), 35 (2004).
[36] T. Nozaki, K. Sasaki, T. Ogino, D. Asahi, K. Okazaki, J. Thermal Science & Technol. **2**(2), 192 (2006).
[37] A. Kunz, P. Roth, Int. J. Chem. Kinet. **33**, 741 (2001).
[38] D. Jurbergs, E. Rogojina, L. Mangolini, U. Kortshagen Appl. Phys. Lett. **88**, 233116-1 (2006).
[39] M. V. Wolkin, J. Jorne, P. M. Fauchet, Phys. Rev. Lett. **82**(1), 197 (1999).

*Corresponding author: tnozaki@mech.titech.ac.jp